WILEY | Hindawi

Research Article

Study of Rock Burst Risk Evolution in Front of Deep Longwall Panel Based on Passive Seismic Velocity Tomography

Kunyou Zhou [ID],[1,2] **Linming Dou** [ID],[1,2] **Siyuan Gong** [ID],[2,3] **Jiazhuo Li** [ID],[2,4] **Jinkui Zhang**,[5] **and Jinrong Cao** [ID][1,2]

[1]*Key Laboratory of Deep Coal Resource Mining, Ministry of Education, China University of Mining and Technology, Xuzhou 221116, China*
[2]*School of Mines, China University of Mining and Technology, Xuzhou 221116, China*
[3]*Laboratory of Mine Earthquake Monitoring and Prevention, China University of Mining and Technology, Xuzhou 221116, China*
[4]*School of Energy and Safety, Anhui University of Science and Technology, Huainan 232001, China*
[5]*Shaanxi Zhengtong Coal Industry Co., Ltd., Xianyang 713600, China*

Correspondence should be addressed to Linming Dou; lmdou@126.com

Monitoring and early-warning are critical for the prevention and controlling of rock burst in deep coal mining. In this study, rock burst risk assessment criterion was built based on the correlativity between seismic velocity and stress state in coal and rock body. Passive seismic velocity tomography using mining-induced seismic waves was conducted regularly and continuously. The evolution of rock burst risk and range in front of a deep longwall panel with folds and adjoining goaf was determined. The influence of pressure-relief measures on rock burst risk was analyzed. The study results indicate that burst risk level and range during panel retreating increase first and then decrease, the peak is reached when it is located at 1# syncline shaft area. When approaching the crossheading, high burst risk zones distribute along the crossheading and further intersect with those in 1# syncline shaft area. Burst risk zones in the inclination of panel show distinct zoning features. Tomography results are in good agreement with the drilling bit result, rock burst occurrence, microseismic activity, and working resistance of hydraulic supports. Pressure-relief measures and mining layout have a distinct influence on burst risk of longwall panel. For prevention and controlling of rock burst risk in deep coal mining, pressure-relief measures should be optimized based on passive tomography results.

1. Introduction

Due to long-term exploitation, coal resources at shallow depths are gradually exhausted, and mining depth of coal is continually increasing. Mining depth in overseas including Poland, Germany, Britain, Japan, and France had already exceeded 1000 m as early as in the 1980s, and now, it has reached 1500 m [1, 2]. Currently, 47 coal mines in China have exceeded 1000 m [3]. With mining depth increasing, the stress state of surrounding rock is continuously deteriorating and rock burst occurs more frequently [4, 5].

Various rock burst mechanisms have been put forward by different methods [6–9]. A universally acknowledged viewpoint is that rock burst is caused by the superposition of dynamic and static stress, as shown in Figure 1. The "contribu-tion rate" of static load and dynamic load for rock burst risk varied with mining depth. Due to high static stress in deep mining, a slight dynamic load increment caused by mining-induced tremor can make superimposed stress exceed the critical value and even lead to a rock burst. Prediction methods for stress field and rock burst risk in deep buried uncertain environments should be further investigated in the future [10].

Seismic velocity tomography, a new geophysical exploration method inferring the wave propagation velocity through structures, has been a novel measurement method for stress redistribution in underground coal mining. Superior to previous methods such as drilling bits [11], pressure sensor [12, 13], electromagnetic emission [14], and acoustic emission [15], seismic velocity tomography can provide comprehensive and continuous stress redistribution by imaging the
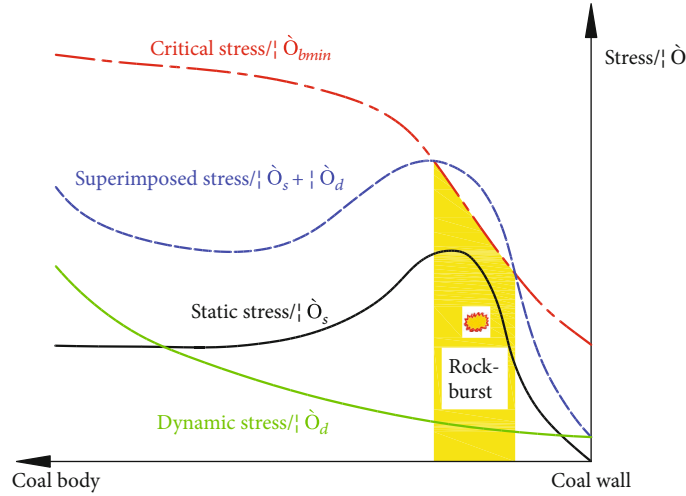
FIGURE 1: Superimposed stress of static and dynamic stress-inducing rock burst.

seismic wave velocity in coal and rock body. Regarding seismic sources, this method can be classified into two types, that is, active velocity tomography and passive velocity tomography [16, 17]. Active velocity tomography has been conducted in geological structure and stress field detection and achieved good results [18–22]. However, due to extra labor and economic cost, the application of active velocity tomography is limited to some extent. Alternatively, passive seismic velocity tomography can rapidly and continuously present the stress redistribution during coal mining by using mining-induced seismicity as the sources seismic wave [23–27]. Passive seismic velocity tomography in existing literatures was mainly used to represent stress redistribution. The relationship between wave velocity change and rock burst risk was rarely inferred.

In this study, a quantitative assessment criterion for rock burst risk was established based on the relation between stress and wave velocity [28–31]. Rock burst risk and range of a deep longwall panel with folds and adjoining goaf were determined continuously and visually based on passive seismic velocity tomography. Moreover, the influence of pressure-relief measures on rock burst risk was analyzed based on tomography results.

2. Theory of Passive Seismic Velocity Tomography for Rock Burst Risk

During the transmission of seismic wave, P-wave is first monitored as it travels faster [23]. P-wave velocity variation with stress under different loading schemes has been conducted in laboratory [28], and it indicates the positive correlation between stress and P-wave velocity. P-wave velocity can reflect stress state and burst risk of rock and coal mass.

A 3D mesh network of mining area is necessary for passive seismic velocity tomography, and mining area is divided into voxels in x, y, and z directions [25, 31]. During the propagation, seismic rays will pass through voxels along the ray path from seismic source to sensors.

Suppose the ray path of the ith seismic wave is L_i and the travel time is T_i, then, the travel time of ith seismic wave from the source to the sensor is the integral of the slowness

S (or the inverse of velocity), which can be expressed by Eq. (1)–Eq. (3) [31–33].

$$V = \frac{L}{T} \rightarrow VT = L, \tag{1}$$

$$T = \int_0^{L_i} \frac{dL}{V(X, Y, Z)} = \int_0^{L_i} S(X, Y, Z)dL, \tag{2}$$

$$T_i = \sum_{j=1}^{M} d_{ij}S_j \, (i = 1, 2, 3\bullet\bullet\bullet\bullet\bullet\bullet\bullet\bullet N), \tag{3}$$

where $V(X, Y, Z)$ is the velocity (m/s), L_i is the ray path of the ith seismic wave (m), T_i is the travel time (s), $S(X, Y, Z)$ is the slowness (s/m), d_{ij} is the distance of the ith ray in the jth voxel, N is the total number of rays, and M is the number of voxels.

Generally, seismic event location and ray path are calculated using an initial velocity model [31]. Due to the unknown velocity, distance, and time in an individual voxel, thus, matrices expressed by Eq. (4) can be built with the voxel slowness, distance, and time. Then, the velocity can be determined by the following matrix [33].

$$T = DS \rightarrow S = D^{-1}T, \tag{4}$$

where T is the travel time per ray matrix ($1 \times N$), D is the distance per ray per voxel matrix ($N \times M$), and P is the slowness per grid cell matrix ($1 \times M$).

Eventually, the key problem of seismic velocity tomography is to solve the slowness vector S. The most effective way to solve this problem is through an iterative process, and the simultaneous iterative reconstructive technique (SIRT) [16, 29, 34] is the famous and effective one, which is adopted in the paper.

Velocity of each voxel can be determined by seismic velocity tomography introduced above. The relationship between seismic velocity anomaly and stress coefficient was given in [30, 31]. In deep coal mining, burst risk is primarily dominated by static stress. Accordingly, an assessment

TABLE 1: Relation between positive velocity anomalies and rock burst risk level.

Rock burst risk index	Rock burst risk level	Positive velocity anomaly, A_n/%
0	None	<5
1	Weak	5-15
2	Middle	15-25
3	Strong	>25

criterion for burst risk in Table 1 is built. Velocity anomaly A_n is determined by

$$A_n = \frac{V_p - V_p^a}{V_p^a}. \tag{5}$$

Where V_p is P-wave velocity in certain voxel, and V_p^a is the average velocity of the model. It should be noted that the zones with positive anomaly and negative anomaly are overstressed and pressure-relieved, respectively [31]. In this paper, the mining area was classified as None, Weak, Middle, and Strong burst risk zones according to rock burst risk assessment criterion in Table 1.

3. Site Characteristics of Selected Longwall Panel

3.1. Geological Conditions. Panel 204 is the fourth fully mechanized caving longwall face in No.2 mining district in a deep coal mine in Shaanxi province, China. The coal mine is seriously threatened by rock burst. Panel 204 is 1455 m long in strike and 200 m wide in inclination, as shown in Figure 2(b). No.4 coal seam, as the single minable seam, has a thickness of 5.9–15.0 m and maximum depth over 1000 m. The coal seam elevation is +72 m–+147 m. Panel 204 was in production in October 2018 and paused from October 2018 to April 2019 due to mine water problem. It was in reproduction in May 2019 and stopped in February 2020 with 850 m advancement. There exist two synclines (named 1# and 2#) and an anticline. 1# and 2# synclines are nearly perpendicular and parallel with the strike of panel 204, respectively. The anticline is 45° oblique with the strike of panel.

There are two inferior key strata and one main key stratum above coal seam, as shown in Figure 2(c). The thickness of key strata is 21.1 m, 54.0 m, and 101.3 m, and the distance to coal seam is 13.4 m, 139.1 m, and 193.1 m, respectively.

No.4 coal seam is of strong burst propensity, and the rock strata in the floor and roof are both of weak burst propensity. The maximum principal stress reaches 38.2-44.8 MPa, and the average uniaxial compressive strength of coal is 19.3 MPa; hence, the stress concentration coefficient is 1.98-2.32, which indicates its high burst risk [35].

3.2. Microseismic Data Acquisition and Processing. A microseismic monitoring system called "SOS," manufactured by Central Mining Institute of Poland, was installed in the coal mine, and the maximum locating errors are 20 m in horizontal direction and 30 m in vertical direction, respectively. Seis-

mic monitoring network in July 2019 is shown in Figure 3. The system has been optimized three times during the panel 204 retreating to ensure the monitoring accuracy. During April 2019 to March 2020, over 3800 mining-induced tremors in No.2 mining district were recorded by SOS. The first arrival time of P-wave in each sensor was calibrated manually till the error between the calculated and theoretical values is less than 20 ms. Some typical tremors in panel 204 are illustrated in Figure 4(b). Seismic wave attenuates by power function as Eq. (6). Seismic waves with higher energy attenuate slower and travel farther, which is consistent with previous studies [36, 37]. Consequently, the quantity and accuracy of microseismic events can satisfy the tomography.

$$V_0(L) = V_{0,\max} L^{-\lambda}. \tag{6}$$

Where L is the distance between tremor and sensor, $V_{0,\max}$ and $V_0(L)$ are the particle velocity at tremor and sensor, respectively, and λ is the attenuation coefficient.

3.3. Inversion Parameters. Tomography area is 2200 m long, 2560 m wide, and 360 m high, which is divided into voxels by 20 m in x and y directions and 30 m in z direction, respectively, as shown in Figure 3. More ray paths enable a higher accuracy in the computation [38]. Thus, only tremors recorded by more than six sensors are considered as seismic sources, and the voxels with more than 10 rays are considered reliable. To improve the efficiency and accuracy of inversion and source locating, SIRT was adopted to recalculate the seismic location, and the slowness in each voxel along the seismic rays was modified by iteration till the threshold value was reached. To start the first iteration and reduce indeterminacy, P-wave initial velocity its range was assumed 4.48 km/s and 3.5 km/s-6.5 km/s, respectively, which was obtained from the P-velocity data in Figure 5.

4. Passive Seismic Velocity Tomography Results

4.1. Rock Burst Risk Evolution with Longwall Panel Retreating. Passive seismic velocity tomography in the mining area was carried out regularly with 2 times per month since May 2019. Thereinto, 8 tomography results of panel 204 are illustrated in Figure 6. Mining-induced tremors in the following one month or half one month are plotted simultaneously to verify the burst risk zones highlighted by tomography. In Figure 6, the velocity anomaly (A_n) in green, yellow, and red area is 0.05-0.15, 0.15-0.25, and >0.25, and the corresponding burst risk is weak, middle, and strong, respectively, based on the rock burst risk criterion given in Table 1.

Notably, panel 205 was in production since November 2019, and tremors were induced in the goaf of panel 204 and abutment area ahead of panel 205, which would bring about seismic rays and high burst risk zones across the goaf. The distance between panels 204 and 205 always exceeds 700 m. Hence, the extraction of panel 205 will not interfere with this study. To illustrate burst risk in front of panel 204 clearly, burst risk zones in the goaf were eliminated artificially.

As clearly shown in Figure 6, the general evolution of rock burst risk and range in front of the face line is closely
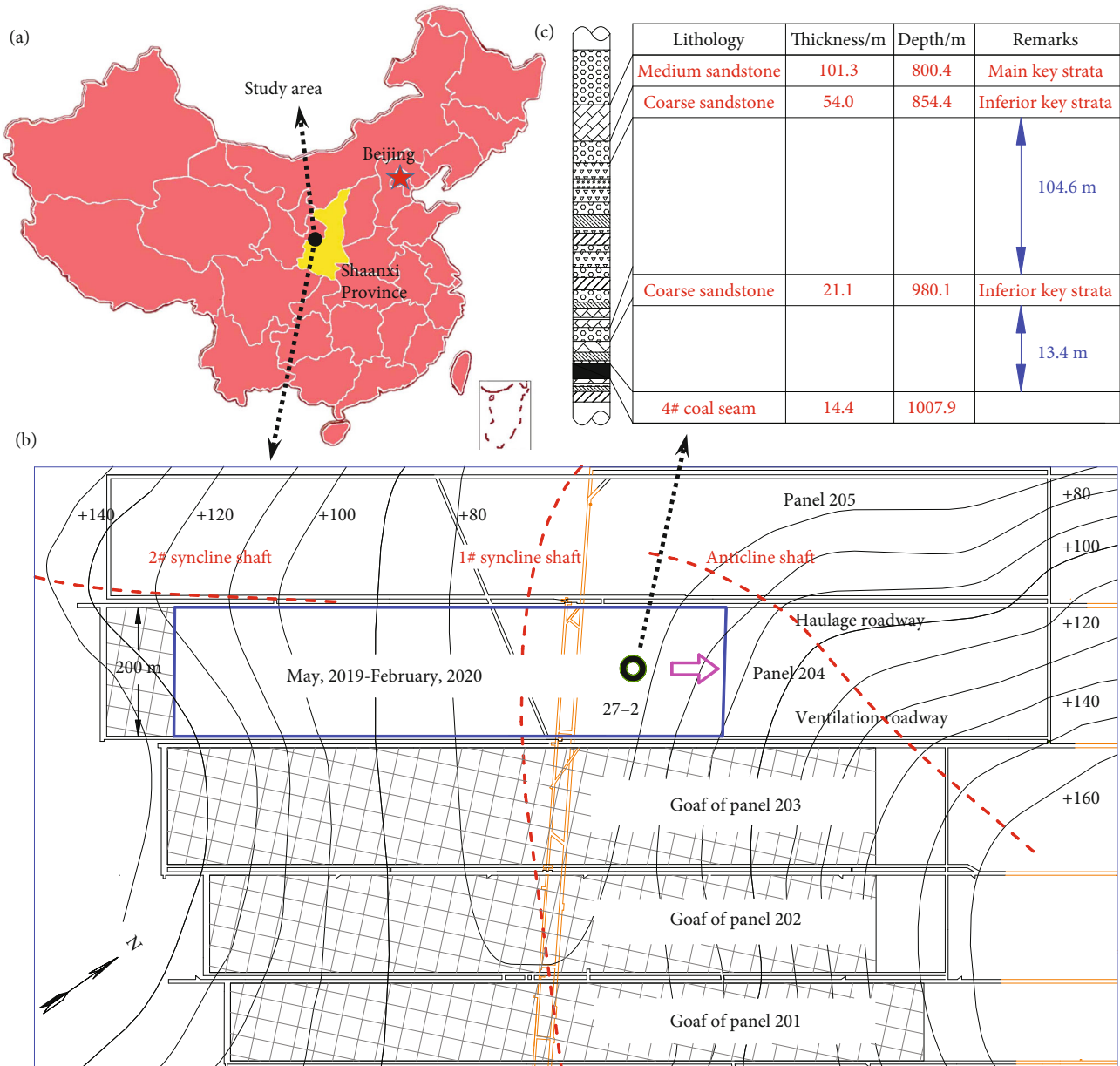
Figure 2: Mining conditions. (a) Location of coal mine. (b) Layout of panel 204. (c) Stratigraphic column of bore 27-2.

Lithology	Thickness/m	Depth/m	Remarks
Medium sandstone	101.3	800.4	Main key strata
Coarse sandstone	54.0	854.4	Inferior key strata
			104.6 m
Coarse sandstone	21.1	980.1	Inferior key strata
			13.4 m
4# coal seam	14.4	1007.9	

related to the retreating of panel 204. High burst risk zone scale ahead of the face line in the strike, including middle and strong burst risk zones, is illustrated in Figure 7. Due to increasingly broadened goaf behind panel 204, goaf of panel 203, and the folds, high burst risk zone scale in front of face line first increases from 60 m, reaches the peak of 410 m, and then decreases to 80 m gradually. The peak is reached when panel located in 1# syncline shaft area in October 2019 (as shown in Figure 6(e)). Burst risk is the highest at that time as well. When the face line is close to the crossheading, high burst risk zones distribute along the crossheading and further intersect with the burst risk zones in 1# syncline area, which indicates the high stress level of the zones adjacent to the crossheading.

In terms of high burst risk along the inclination of panel 204, the range of burst risk zones on the ventilation roadway side is always larger than that on the haulage roadway side. However, the evolution of high burst risk shows distinct zoning features. Hence, the mining process of panel 204 can be divided into 3 phases along the strike, as shown in Figure 8.

(i) *Phase 1*. May 2019-July 2019, during this period, high burst risk zones (zone 1) are mainly lying beside the haulage roadway, as shown in Figures 6(a) and 6(b), which could be caused by the tectonic stress of 2# syncline and the coal seam dip angle change

(ii) *Phase 2*. August 2019-December 2019, in this phase, high burst risk zones (zone 2 and 3) are mainly lying beside the ventilation roadway and the vicinity of the cross heading and 1# syncline shaft beside the haulage roadway, respectively, as seen in Figures 6(c)–6(f).
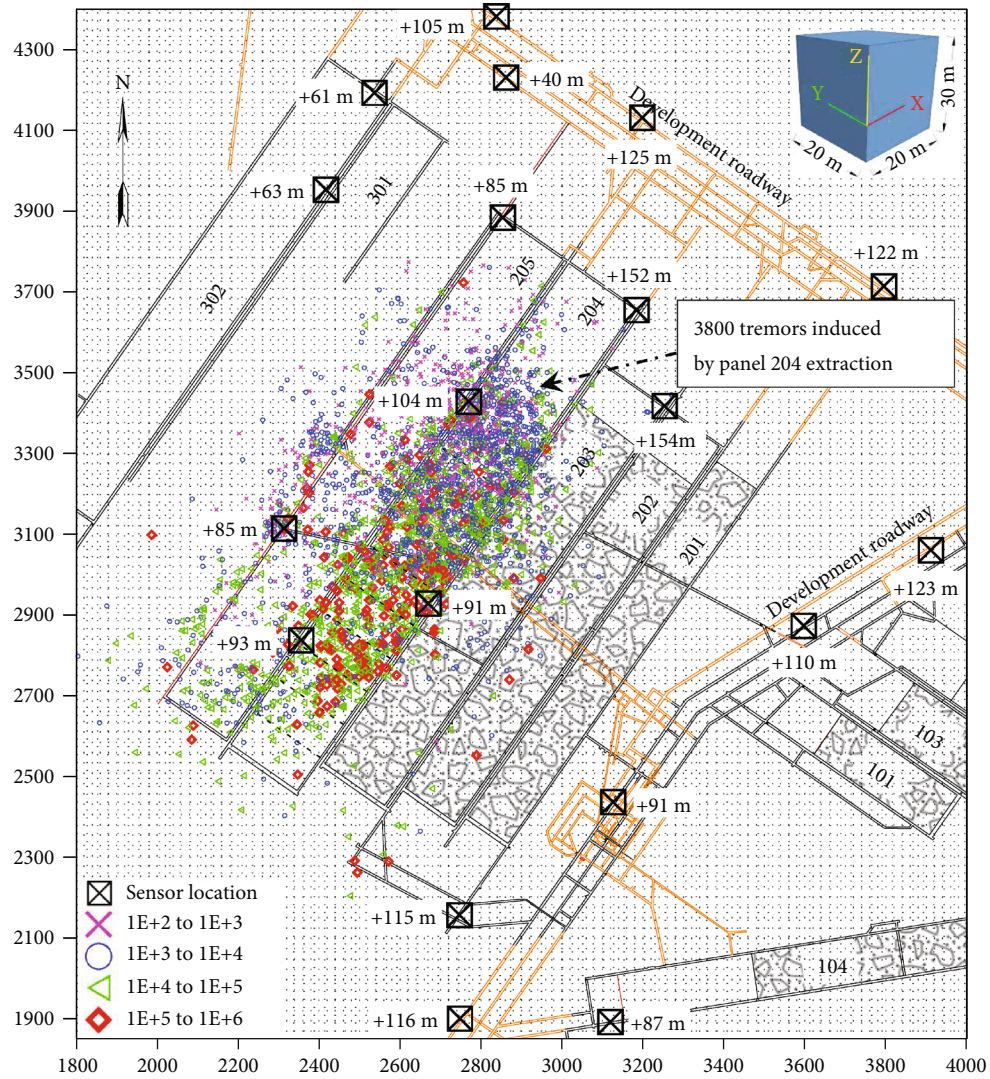
Figure 3: Seismic monitoring network and mining-induced tremors distribution.

Zone 2 could be caused by the tectonic stress of 1# syncline, side abutment stress of panel 203 goaf, and the abutment stress of crossheading. Zone 3 could be caused by the tectonic stress of 1# syncline and the abutment stress of crossheading

(iii) *Phase 3.* January 2020-March 2020, as for this phase, high burst risk zones (zone 4) are mainly lying beside the haulage roadway, as seen in Figures 6(g) and 6(h), which could be caused by the tectonic stress of the anticline and coal seam dip angle change

Moreover, the distribution of mining-induced tremors over 1E4 J in the following mining period (one month or half one month after tomography) are well corresponding to high burst risk zones determined by the previous tomography above.

4.2. Validation of Tomography Results

4.2.1. Drilling Bits. Tomography results on 30 April 2019 (Figure 6(a)) indicate that burst risk zones along the ventila-

tion roadway are mainly located at 95 m-255 m and 340 m-560 m in front of the face line. Particularly, strong burst risk zones are about 200 m away from the face line.

Total 16 drilling bits boreholes with 10 m in depth and 42 mm in diameter were drilled in 15 m-255 m in front of face line in ventilation roadway on 1-2 May 2019. Pulverized coal results are illustrated in Figure 9(b). High pulverized zones are lying in 110 m-170 m and 180 m-230 m ahead of face line, respectively. The peak is located at 210 m ahead of the face line. Drilling bits results are well corresponding to burst risk zones in Figure 6(a).

4.2.2. Rock Burst Occurrence. A rock burst occurred in 20 m-140 m on 21 September 2019, and meanwhile, a tremor of 4.6×10^5 J was recorded at 18 m in front of the face line on the haulage roadway side, as shown in Figure 10. The floor of haulage roadway heaves for 1.5 m in average and the cross-section of roadway shrinks sharply, which leads to a 4 days shutdown of panel 204. Furthermore, the tremor is at the intersection between weak and middle risk zones, and rock burst areas are
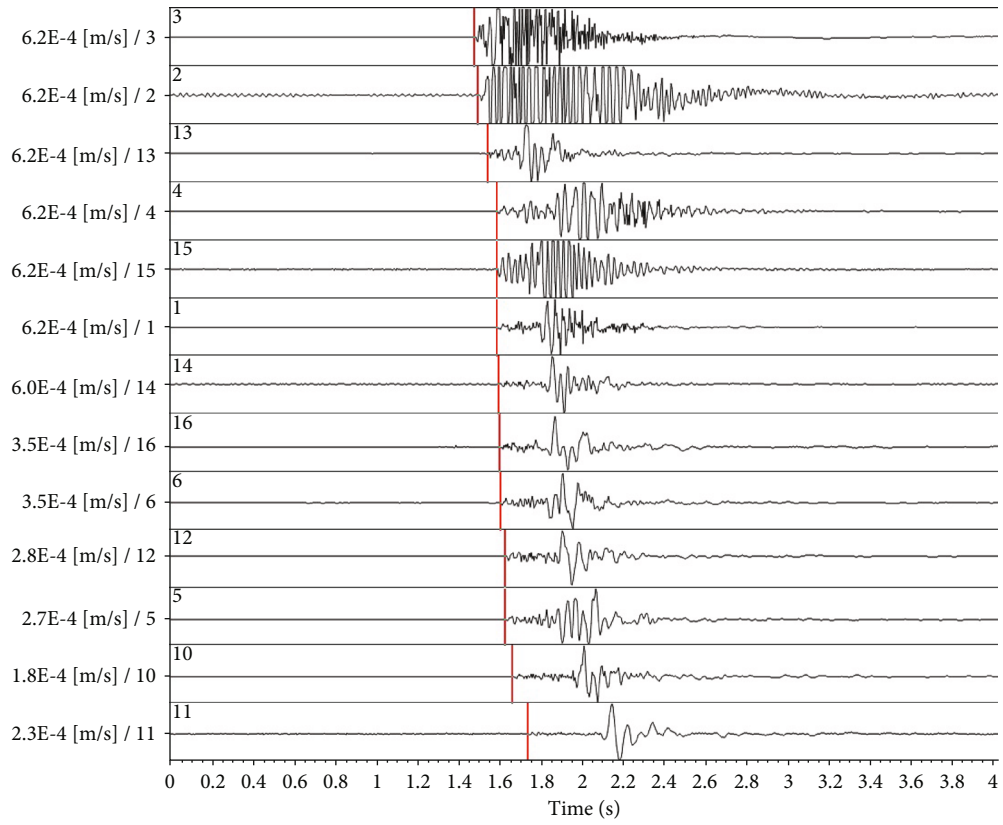
(a)
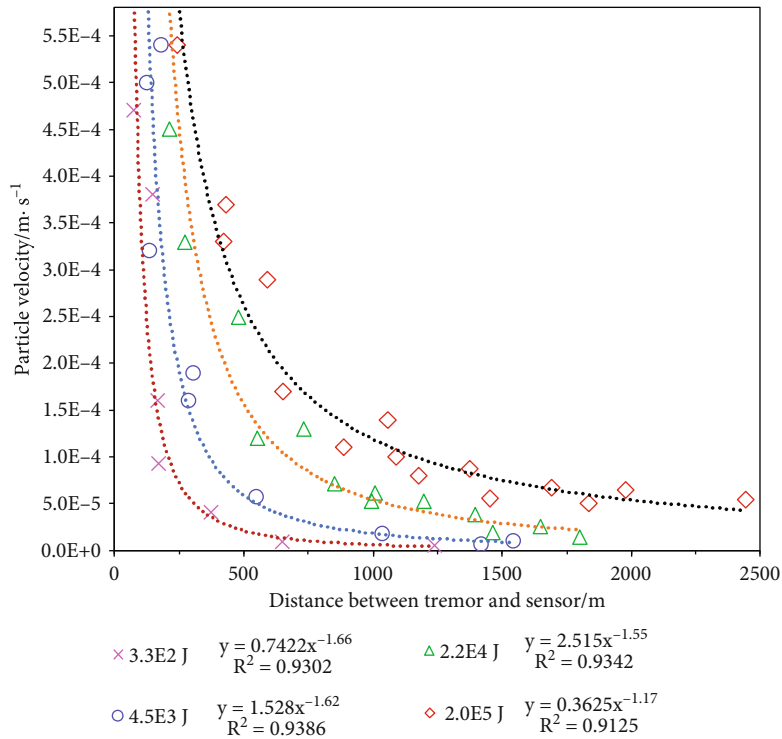
(b)

Figure 4: Calibration of the P-wave arrival time and typical seismic wave attenuation characteristics.
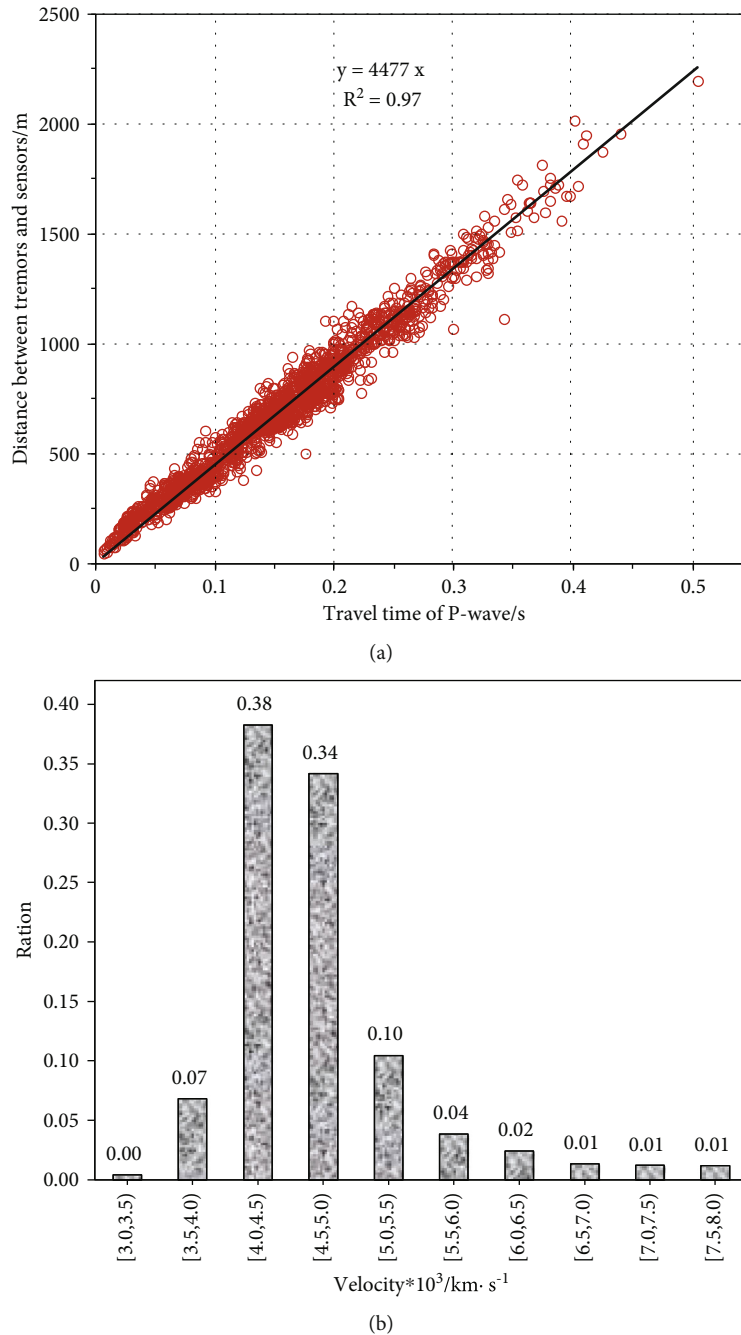
(a)

(b)

FIGURE 5: Seismic velocity statistics of the seismic rays in panel 204.

in the middle and strong burst risk zones determined by the tomography on 15 September 2019. The typical rock burst area matches well with the tomography result.

4.2.3. Microseismic Activity. According to Figure 6 in Section 4.1, mining-induced tremors over 1E4 J in the following period are well corresponding to the former tomography results. Moreover, microseismic activity of panel 204 from May 2019 to March 2020 is depicted in Figure 11. And it gradually increases since panel 204 is in reproduction, reaches the peak in October 2019, and then decreases rapidly.

In October 2019, panel 204 is retreated in 1# syncline shaft area. Microseismic activity is well consistent with rock burst risk evolution in time sequence.

4.2.4. Working Resistance of Hydraulic Supports. Working resistance contour of hydraulic supports in panel 204 is shown in Figure 12. It should be noted that panel 204 was out of working from 21 January 2020 to 3 February 2020. The working resistance of hydraulic supports, on the whole, is increasing gradually and decreasing subsequently along the strike direction, which is similar to the
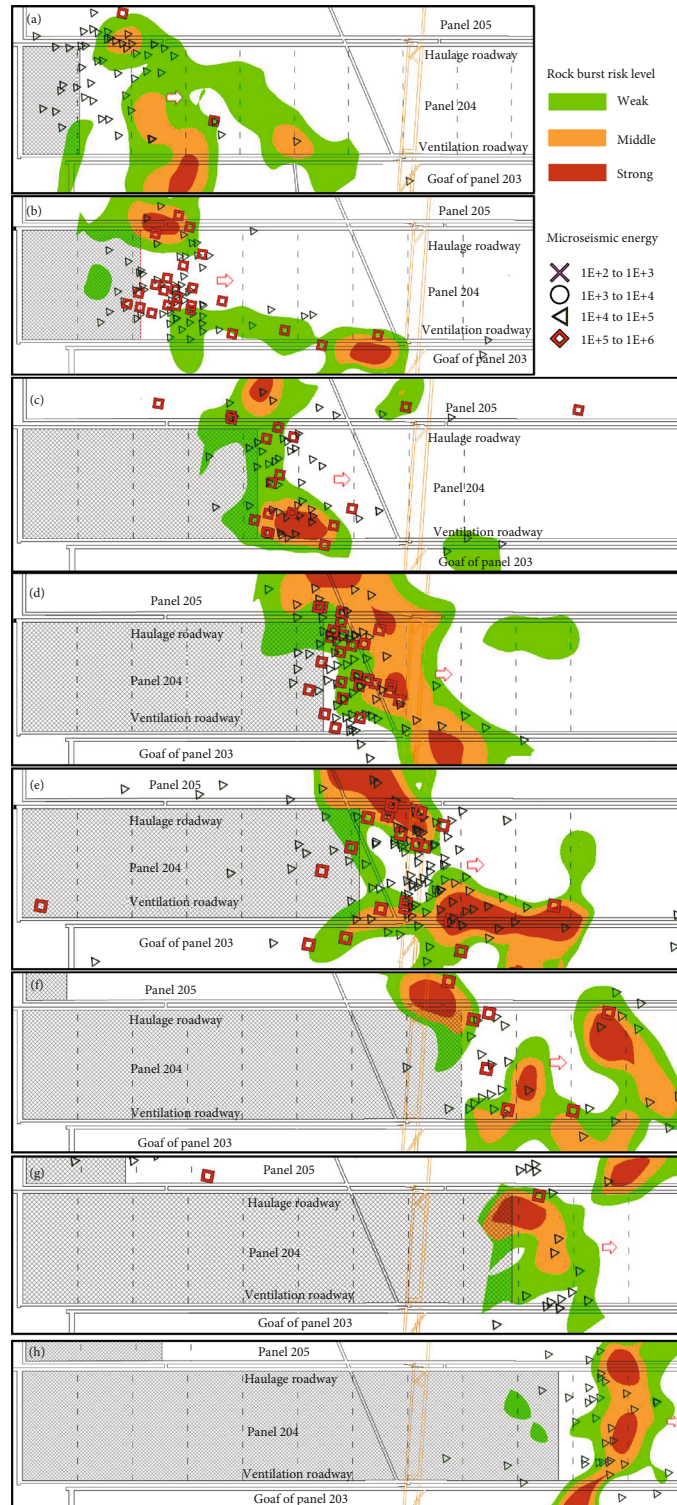
FIGURE 6: Rock burst risk zones and future seismic events. (a) Burst risk zones on 30 April 2019 and seismic events from 1 to 30 May 2019. (b) Burst risk zones on 31 May 2019 and seismic events from 1 to 30 June 2019. (c) Burst risk zones on 31 July 2019 and seismic events from 1 to 31 August 2019. (d) Burst risk zones on 15 September 2019 and seismic events from 16 to 30 September 2019. (e) Burst risk zones on 15 October 2019 and seismic events from 16 to 31 October 2019. (f) Burst risk zones on 15 December 2019 and seismic events from 16 December 2019 to 15 January 2020. (g) Burst risk zones on 31 January 2020 and seismic events from 1 to 15 February 2020. (h) Burst risk zones on 29 February 2020 and seismic events from 1 to 15 March 2020.
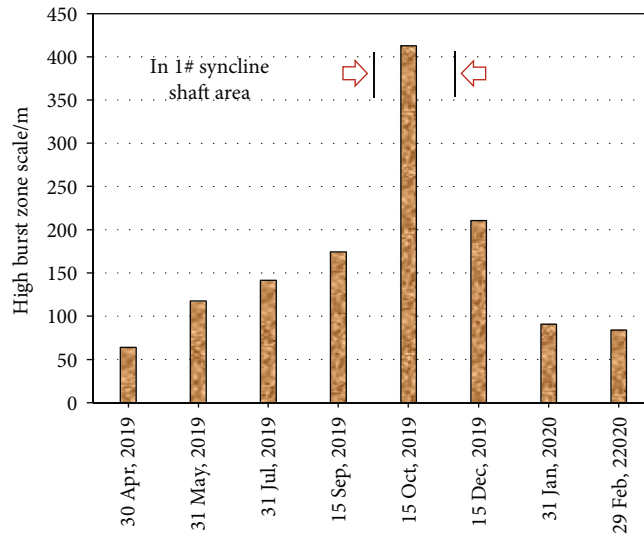
FIGURE 7: High burst zone scale (middle and strong burst zone) in front of the face line.
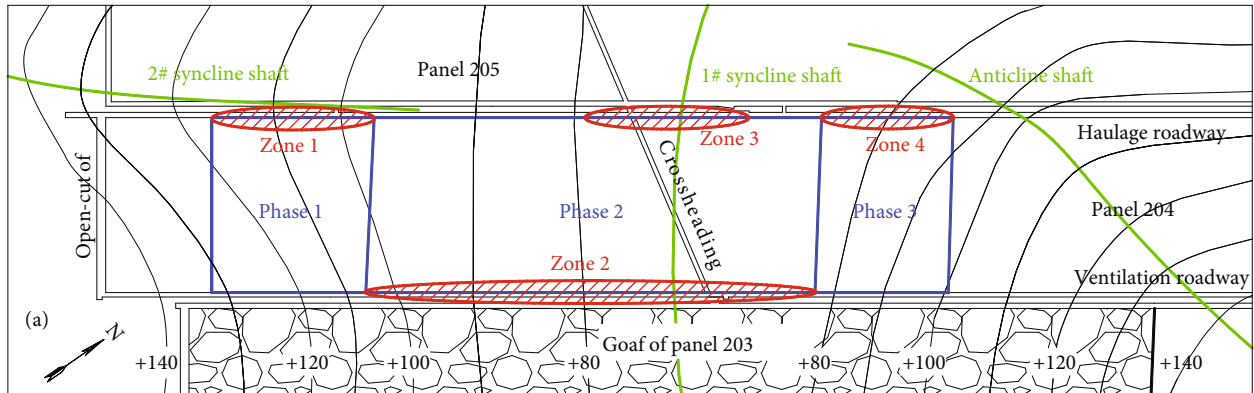

FIGURE 8: Burst risk zoning features of panel 204 and the filled ellipses indicate high burst risk zones.
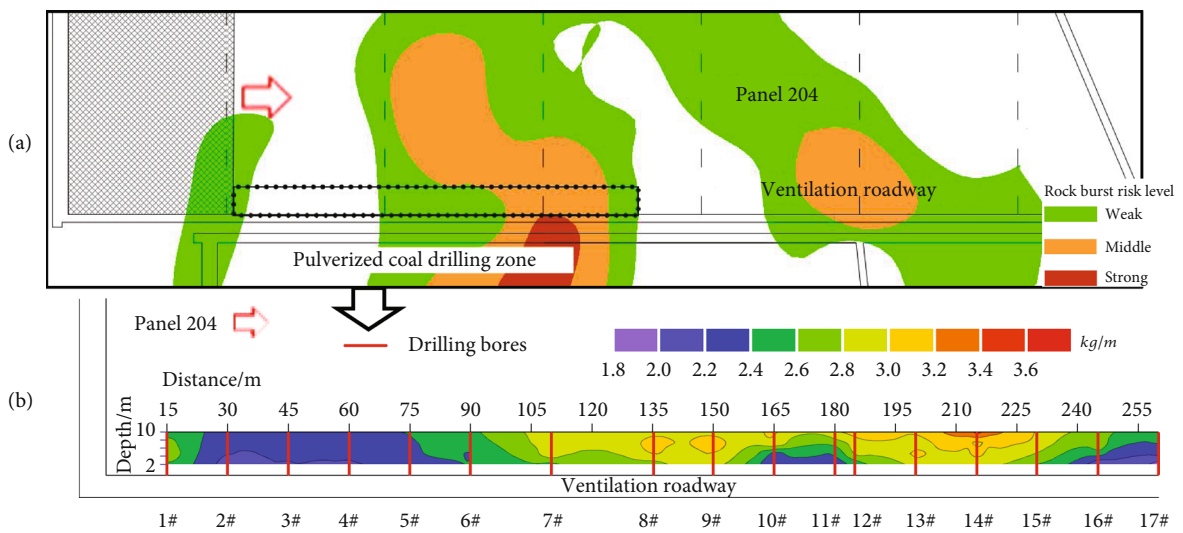

FIGURE 9: Rock burst risk zones on 30 April and drilling bits results on 1-2 May 2019.
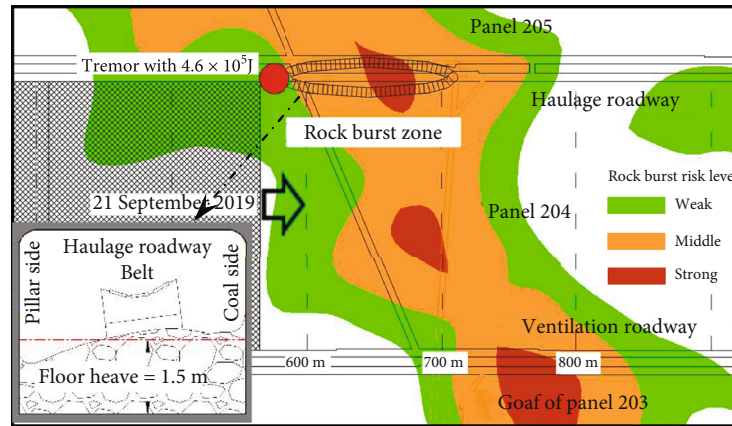
Figure 10: Rock burst zones on 15 September 2019 and rock burst occurred on 21 September 2019.
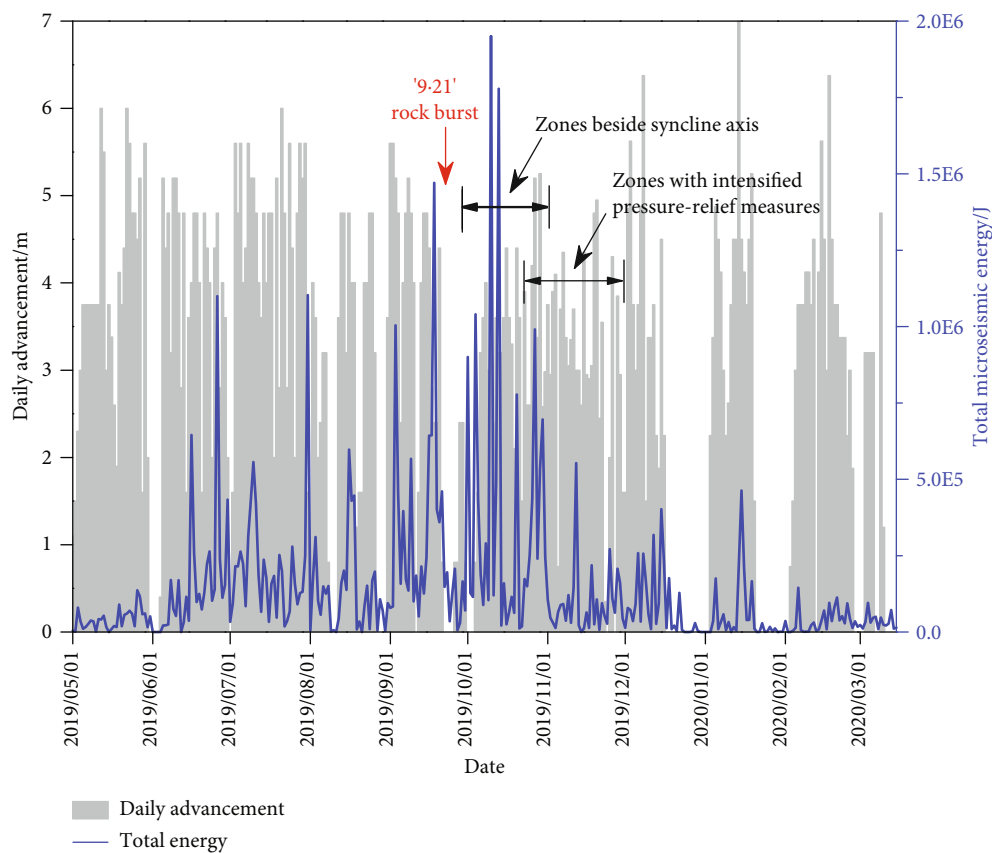

Figure 11: Microseismic activity of panel 204 between 1 May 2019 and 15 March 2020.

microseism activity in Figure 11. In addition, from May to June 2019, high working resistance zones are mainly located on the haulage roadway side, and it is identical to the high burst risk zones in Figures 6(a) and 6(b). From September to November 2019, high working resistance zones are mainly distributed on the ventilation roadway side, and it is identical to the high burst risk zones in Figures 6(c)–6(f). From January to March 2020, high working resistance zones are mainly on the haulage roadway side, which is identical to the high burst risk zones in Figures 6(g) and 6(h).

In summary, the field drilling bit results, rock burst occurrence, microseism activity, and working resistance of hydraulic supports are well identical to the tomography results, which indicate the feasibility and accuracy of passive seismic velocity tomography for rock burst risk.

4.3. Influence of Pressure-Relief Measures on Rock Burst Risk.
Zones in 0 m-250 m ahead of panel 204 were intensified pressure-relieved with deep presplitting blasting, coal blasting in coal wall and floor since rock burst occurrence on 21 September 2019. In November 2019, panel 204 was extracted
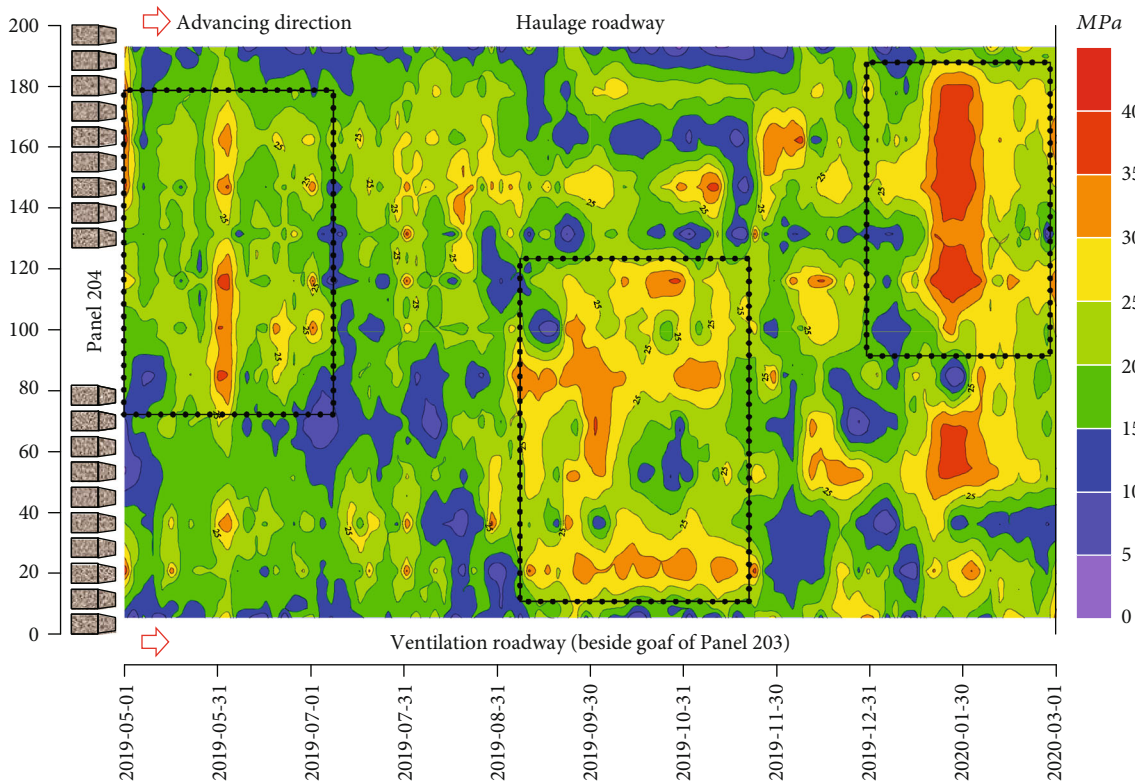
Figure 12: Working resistance of hydraulic supports in panel 204 from May 2019 to February 2020.
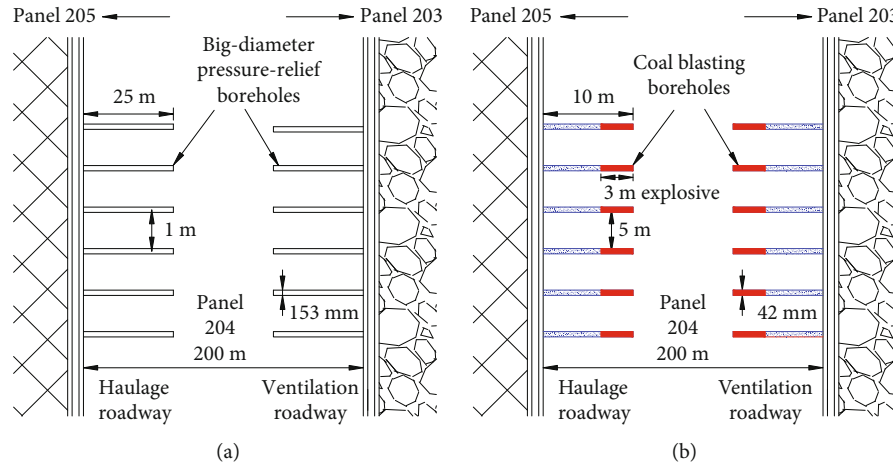

Figure 13: Schematic diagram of pressure-relief measures in the coal wall of panel 204: (a) big-diameter pressure-relief boreholes; (b) coal blasting boreholes.

in the intensified pressure-relief zones, and the microseismic activity decreased obviously (as shown in Figure 11), which indicates that pressure-relief measures have a significant influence on rock burst risk.

To investigate the influence of pressure-relief measures on rock burst risk visually and quantitatively, pressure-relief measures and zones in panel 204 from September 2018 to May 2019 were analyzed, and three passive tomographies were conducted in early May 2019.

Big-diameter borehole is the primary pressure prerelief method. Secondary big-diameter boreholes or coal blasting

boreholes will be implemented again at interval of primary boreholes if the risk is not effectively eliminated. Big-diameter borehole is 153 mm in diameter, 25 m in depth, and 1 m in interval. Coal blasting borehole is 42 mm in diameter, 10 m in depth, 5 m in interval, 1.2 m from the floor, and charged with 3 kg explosive, as shown in Figure 13.

As illustrated in Figure 14(a), before 1 May 2019, the zones 0-255 m and 295 m-490 m ahead of face line on haulage roadway side and 0 m-165 m and 270 m-320 m ahead of face line on ventilation roadway side were pressure-relieved with big-diameter boreholes. And further, the zones 125 m-
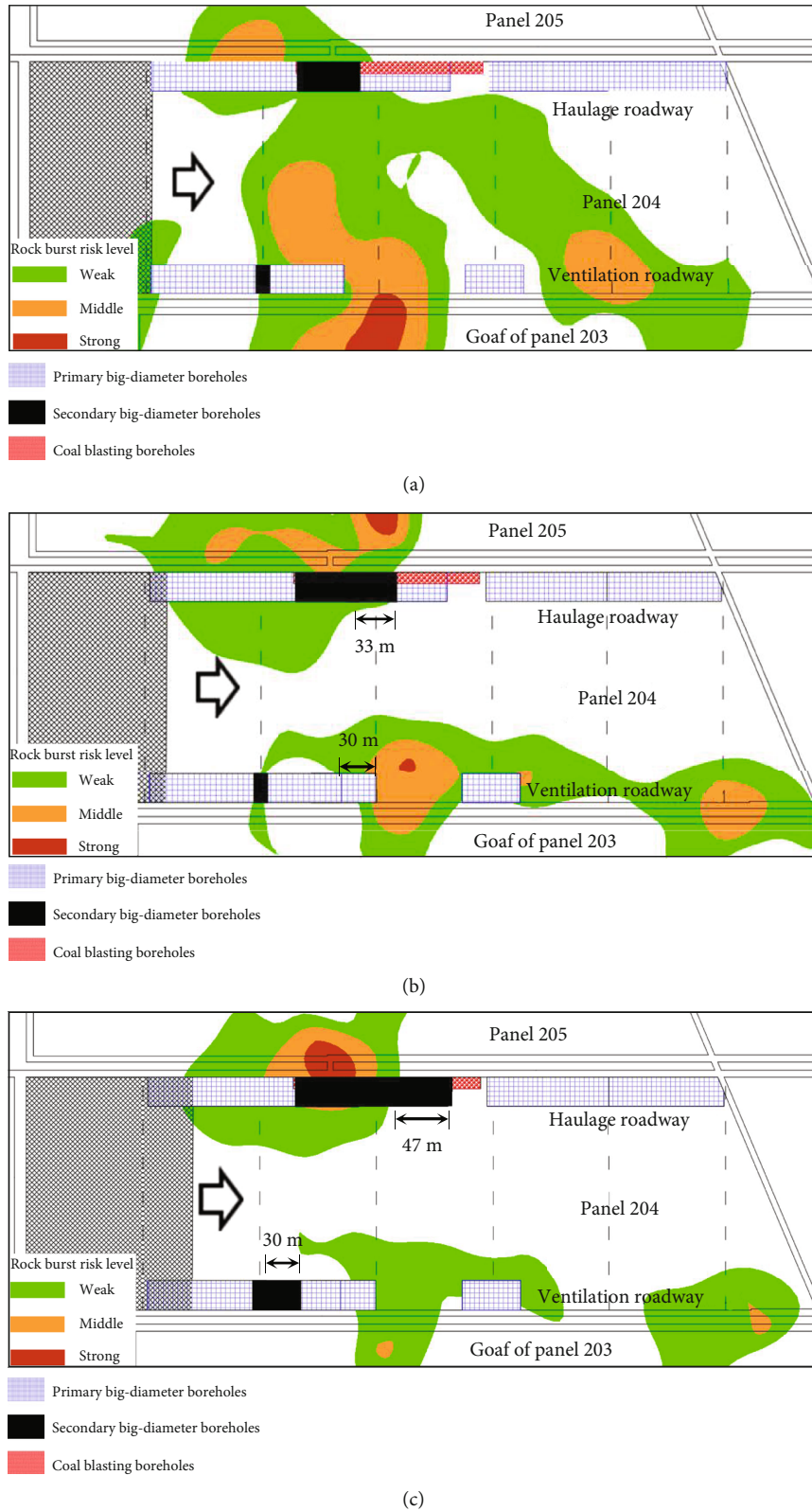
(a)

(b)

(c)

FIGURE 14: Rock burst risk zones and pressure-relieved zones in panel 204. (a) 30 April 2019. (b) 6 May 2019. (c) 12 May 2019.

285 m ahead of face line on haulage roadway side were pressure-relieved with coal blasting. Tomography results on 30 April, 6 May, and 12 May 2019 are shown in Figure 14. Figure 14(a) illustrates that pressure-relieved zones match well with the low burst risk zones except for the zones 0 m-200 m ahead of the face line on the haulage roadway side. In the following six days, 33 and 30 big-diameter boreholes were carried out at haulage and ventilation roadway,

respectively. Then, the corresponding high burst risk zones are dispelled obviously, as shown in Figure 14(b). From 7 May to 12 May, 47 and 30 boreholes were drilled at haulage and ventilation roadway, respectively. Similarly, the corresponding burst risk zones are eliminated as well, especially for the zones on the ventilation roadway side, as shown in Figure 14(c).

Generally, with production, stress field is adjusted; high stress and burst risk zones are shifted closer to the face line in the strike direction and to haulage or ventilation roadway in the inclination direction. Stress level and burst risk increase simultaneously. However, burst risk zones on the ventilation roadway side, contrarily, are being away from the face line. Burst risk eliminated zones match well with the pressure-relieved area, which indicates that pressure-relief measures and intensity in ventilation roadway can decrease burst risk effectively. However, high burst risk in zones 200 m in front of the face line on the haulage roadway side is not eliminated substantially, which is further proved by the future tremors in May 2019 as shown in Figure 6(a). Hence, more pressure-relief measures, such as coal blasting or deep presplitting blasting in roof, should be adopted till the risk is eliminated thoroughly. Therefore, pressure-relief measures have a distinct influence on stress field and burst risk of panel, which can account for the none or weak burst risk zones closely ahead of the face line in Figure 6. And moreover, passive seismic velocity tomography before and after the pressure-relief measures implemented can be a novel and effective method to assess pressure-relief effect.

5. Conclusion

Based on passive seismic velocity tomography results and rock burst risk assessment criterion, the burst risk and range evolution of a deep longwall panel were determined, and the influence of pressure-relief measures on burst risk was analyzed. The main conclusions are as follows:

(1) Seismic wave propagation velocity in rock and coal mass is in positive correlation with the stress level. Seismic wave velocity distribution of rock and coal mass can be used to assess the rock burst risk in deep coal mining. And accordingly, a rock burst risk assessment criterion with velocity analogy was built

(2) Passive tomography results indicate that due to the tectonic stress, abutment pressure, and mining layout, rock burst risk and range of the deep panel firstly increase, then decrease, and reach the peak at the 1# syncline shaft area during panel retreating. High burst risk zones in the inclination of panel show distinct zoning features. When panel approaching the crossheading, high burst risk zones distribute along the crossheading and further intersect with the burst risk zones in 1# syncline shaft area

(3) High burst risk zones identified by passive seismic velocity tomography are well correlated with drilling bits results, rock burst records, microseism activity, and the working resistance of hydraulic supports, which indicates the practicability and accuracy of passive tomography for rock burst risk in deep coal mining

(4) Pressure-relief measures and mining layout of panel have a distinct influence on rock burst risk, which can be assessed by passive seismic velocity tomography. Pressure-relief measures and intensity in different mining phases should be optimized timely based on the tomography results

Data Availability

The figures and tables used to support the findings of this study are included in the article.

Conflicts of Interest

The authors declare no conflict of interest.

Acknowledgments

References

[1] H. P. Xie, F. Gao, Y. Ju et al., "Quantitative definition and investigation of deep mining," *Journal of China Coal Society*, vol. 40, no. 1, pp. 1–10, 2015.

[2] P. G. Ranjith, J. Zhao, M. H. Ju, R. V. S. de Silva, T. D. Rathnaweera, and A. K. M. S. Bandara, "Opportunities and challenges in deep mining: a brief review," *Engineering*, vol. 3, no. 4, pp. 546–551, 2017.

[3] M. C. He, *Investigation on the Typical Rock Burst Coal Mines with 1000m Depth*, Beijing, National Coal Mine Safety Administration, 2019.

[4] H. P. Xie, H. W. Zhou, D. J. Xue, H. W. Wang, R. Zhang, and F. Gao, "Research and consideration on deep coal mining and critical mining depth," *Journal of China Coal Society*, vol. 37, no. 37, pp. 535–542, 2012.

[5] Q. X. Qi, Y. S. Pan, L. Y. Shu et al., "Theory and technical framework of prevention and control with different sources in multi-scales for coal and rock dynamic disasters in deep mining of coal mines," *Journal of China Coal Society*, vol. 43, no. 7, pp. 1801–1810, 2018.

[6] L. M. Dou, X. Q. He, T. Ren, J. He, and Z. Y. Wang, "Mechanism of coal-gas dynamic disasters caused by the superposition of static and dynamic loads and its control technology," *Journal of China University of Mining & Technology*, vol. 47, no. 1, pp. 48–59, 2018.

[7] T. H. Ma, C. A. Tang, S. B. Tang et al., "Rockburst mechanism and prediction based on microseismic monitoring," *International Journal of Rock Mechanics and Mining Sciences*, vol. 110, pp. 177–188, 2018.

[8] W. C. Zhu, Z. H. Li, L. Zhu, C. A. Tang, and C. A. Tang, "Numerical simulation on rockburst of underground opening triggered by dynamic disturbance," *Tunnelling and Underground Space Technology*, vol. 25, no. 5, pp. 587–599, 2010.

[9] X. H. Yang, T. Ren, and L. H. Tan, "Estimation of average ejection velocity generated by rib burst under compression load," *International Journal of Rock Mechanics and Mining Sciences*, vol. 128, article 104277, 2020.

[10] W. Liang, B. Dai, G. Zhao, and H. Wu, "A Scientometric review on rockburst in hard rock: two decades of review from 2000 to 2019," *Geofluids*, vol. 2020, Article ID 8763283, 17 pages, 2020.

[11] S. T. Gu, C. Q. Wang, B. Y. Jiang, Y. L. Tan, and N. N. Li, "Field test of rock burst danger based on drilling pulverized coal parameters," *Disaster Advances*, vol. 5, no. 4, pp. 237–240, 2012.

[12] A. K. Singh, R. Singh, J. Maiti, R. Kumar, and P. K. Mandal, "Assessment of mining induced stress development over coal pillars during depillaring," *International Journal of Rock Mechanics & Mining Sciences*, vol. 48, no. 5, pp. 805–818, 2011.

[13] D. C. Wang, Q. Wang, S. C. Li et al., "Stress distribution characteristics of deep mine in fully-mechanized sublevel caving face based on microseismic and online stress monitoring system," *Journal of Mining & Safety Engineering*, vol. 32, no. 3, pp. 382–388, 2015.

[14] X. Q. He, W. X. Chen, B. S. Nie, and H. Mitri, "Electromagnetic emission theory and its application to dynamic phenomena in coal-rock," *International journal of rock mechanics & mining sciences*, vol. 48, no. 8, pp. 1352–1358, 2011.

[15] Z. Z. Zhang, F. Gao, and X. J. Shang, "Rock burst proneness prediction by acoustic emission test during rock deformation," *Journal of Central South University*, vol. 21, no. 1, pp. 373–380, 2014.

[16] K. Luxbacher, E. Westman, P. Swanson, and M. Karfakis, "Three-dimensional time-lapse velocity tomography of an underground longwall panel," *International Journal of Rock Mechanics & Mining Sciences*, vol. 45, no. 4, pp. 478–485, 2008.

[17] S. C. Maxwell and R. P. Young, "A comparison between controlled source and passive source seismic velocity images," *Bulletin of the Seismological Society of America*, vol. 83, no. 6, pp. 1813–1834, 1993.

[18] M. J. Friedel, M. J. Jackson, E. M. Williams, M. S. Olson, and E. Westman, "Tomographic imaging of coal pillar conditions: observations and implications," *International Journal of Rock Mechanics and Mining Science & Geomechanics Abstracts*, vol. 33, no. 3, pp. 279–290, 1996.

[19] S. P. Peng, B. C. Ling, and S. D. Liu, "Application of seismic tomography in longwall top-coal caving face," *Chinese Journal of Rock Mechanics and Engineering*, vol. 21, no. 12, pp. 1786–1790, 2002.

[20] L. Z. Du, X. P. Zhang, J. J. Niu, X. G. Wang, and G. L. Feng, "The seismic CT method in measuring rock bodies," *Applied Geophysics*, vol. 3, no. 3, pp. 192–195, 2006.

[21] H. He, L. M. Dou, X. W. Li, Q. Q. Qiao, T. J. Chen, and S. Y. Gong, "Active velocity tomography for assessing rock burst hazards in a kilometer deep mine," *Mining Science and Technology (China)*, vol. 21, no. 5, pp. 673–676, 2011.

[22] W. Cai, L. Dou, A. Cao, S. Gong, and Z. Li, "Application of seismic velocity tomography in underground coal mines: a case study of Yima mining area, Henan, China," *Journal of Applied Geophysics*, vol. 109, pp. 140–149, 2014.

[23] E. C. Westman, K. Y. Haramy, and A. D. Rock, "Seismic tomography for longwall stress analysis," in *Proceedings of the 2nd North American Rock Mechanics Symposium*, pp. 397–403, Montreal, Rotterdam, Balkema, 1996.

[24] S. Nakagawa, K. T. Nihei, and L. R. Myer, "Shear-induced conversion of seismic waves across single fractures," *International Journal of Rock Mechanics and Mining Sciences*, vol. 37, no. 1-2, pp. 203–218, 2000.

[25] N. Hosseini, K. Oraee, K. Shahriar, and K. Goshtasbi, "Studying the stress redistribution around the longwall mining panel using passive seismic velocity tomography and geostatistical estimation," *Arabian Journal of Geosciences*, vol. 6, no. 5, pp. 1407–1416, 2013.

[26] X. Ma, E. Westman, D. Counter, F. Malek, and B. Slaker, "Passive seismic imaging of stress evolution with mining-induced seismicity at hard-rock deep mines," *Rock Mechanics and Rock Engineering*, vol. 53, no. 6, pp. 2789–2804, 2020.

[27] J. Vatcher, S. D. Mckinnon, and J. Sjoberg, "Rock mass characteristics and tomographic data," *Rock Mechanics and Rock Engineering*, vol. 51, no. 5, pp. 1615–1619, 2018.

[28] S. Y. Gong, L. M. Dou, J. He, H. He, C. P. Lu, and Z. L. Mu, "Study of correlation between stress and longitudinal wave velocity for deep burst tendency coal and rock samples in uniaxial cyclic loading and unloading experiment," *Rock and Soil Mechanics*, vol. 33, no. 1, pp. 41–47, 2012.

[29] N. Hosseini, K. Oraee, K. Shahriar, and K. Goshtasbi, "Passive seismic velocity tomography on longwall mining panel based on simultaneous iterative reconstructive technique (SIRT)," *Journal of Central South University*, vol. 19, no. 8, pp. 2297–2306, 2012.

[30] L. M. Dou, W. Cai, S. Y. Gong, R. J. Han, and J. Liu, "Dynamic risk assessment of rock burst based on the technology of seismic computed tomography detection," *Journal of China Coal Society*, vol. 39, no. 2, pp. 238–244, 2014.

[31] A. Y. Cao, L. M. Dou, W. Cai, S. Y. Gong, S. Liu, and G. C. Jing, "Case study of seismic hazard assessment in underground coal mining using passive tomography," *International Journal of Rock Mechanics and Mining Sciences*, vol. 78, pp. 1–9, 2015.

[32] H. Navid, "Evaluation of the rockburst potential in longwall coal mining using passive seismic velocity tomography and image subtraction technique," *Journal of Seismology*, vol. 21, no. 5, pp. 1101–1110, 2017.

[33] S. Y. Gong, J. Li, F. Ju, L. M. Dou, J. He, and X. Y. Tian, "Passive seismic tomography for rockburst risk identification based on adaptive-grid method," *Tunneling & Underground Space Technology*, vol. 86, pp. 198–208, 2019.

[34] P. Gilbert, "Iterative methods for the three-dimensional reconstruction of an object from projections," *Journal of Theoretical Biology*, vol. 36, no. 1, pp. 105–117, 1972.

[35] G. A. Zhu, L. M. Dou, and Z. W. Ding, "Experimental study on rock burst of coal samples under overstress and triaxial unloading," *Journal of China Coal Society*, vol. 43, no. 5, pp. 1258–1271, 2018.

[36] B. Liu, C. P. Lu, L. M. Dou, H. Liu, and B. B. Du, "Simulation study on shock wave propagation character in coal and rock," *Journal of China Coal Society*, vol. 36, suplement. 2, pp. 247–253, 2011.

[37] A. Y. Cao, X. Luo, L. M. Dou, H. H. Wang, and K. Andrew, "Experimental research on seismic wave transmission and attenuation associated with underground longwall coal mining," *Journal of Mining & Safety Engineering*, vol. 28, no. 4, pp. 530–535, 2011.

[38] G. K. Ghosh and C. Sivakumar, "Application of underground microseismic monitoring for ground failure and secure longwall coal mining operation: a case study in an Indian mine," *Journal of Applied Geophysics*, vol. 150, pp. 21–39, 2018.